14th International Conference on Structural Safety and Reliability - ICOSSAR'25
1-6 June, 2025 - Los Angeles California, USA
R. Ghanem, E. Johnson, S. Masri and A. Olivier (Eds)

RELIABILITY ANALYSIS OF FLOATING OFFSHORE WIND TURBINE STRUCTURE UNDER EXTREME WIND-WAVE LOADS USING THE HYBRID TMDI

TONG CHANG[1], YONGBO PENG[2] AND YIFENG LIN[3]

[1] State Key Laboratory of Disaster Reduction in Civil Engineering, Tongji University, Shanghai, P.R. China
College of Civil Engineering, Tongji University, Shanghai, P.R. China
200092
tongchang@tongji.edu.cn

[2] State Key Laboratory of Disaster Reduction in Civil Engineering, Tongji University, Shanghai, P.R. China
Shanghai Institute of Disaster Prevention and Relief, Tongji University, Shanghai, P.R. China
200092
pengyongbo@tongji.edu.cn and https://www.researchgate.net/profile/Yongbo-Peng

[3] Shanghai Investigation of Design & Research Institute Co. Ltd, Shanghai, P. R China
200335
Lyf@sidri.com

Key words: Numerical simulations, typhoon events, reliability analysis, tuned mass-damper-inerter (TMDI), hybrid control

Abstract. The optimized control device effectively mitigates adverse vibrations in the floating offshore wind turbine structure induced by external environmental conditions. However, the deep-offshore environment is complex and exhibits high variability, especially during extreme events such as typhoons. Therefore, it is challenging to obtain optimal design parameters for the control device installed on the floating offshore wind turbine by only considering a single sea state or one extreme event. For illustrative purposes, based on a parameterized wind-wave field model combined with the CMA Tropical Cyclone Best Track Dataset and ERA5 measured data, two typical super-typhoon scenarios in a specific sea area were simulated. The vibration mitigation performance of the FOWT structure under extreme conditions was analyzed. Numerical results show that the cumulative distribution functions (CDFs) of extreme structural responses for the floating offshore wind turbine exhibit significant differences under different typhoon events. Additionally, they indicate that to ensure the robustness of the control device, the design must account for the impact of many typhoons in the entire sea area affecting the specific site.

1 INTRODUCTION

Unlike fixed-bottom wind turbines, floating offshore wind turbines (FOWTs) feature degrees of freedom in their base motions, including surge, sway, heave, roll, pitch, and yaw. These motions introduce additional dynamics, such as fore-aft and lateral oscillations of the tower structure, along with corresponding platform movements. Consequently, the support tower and pitch actuators endure substantial fatigue damage equivalent loads (FDELs) and oscillations, resulting in problems like output power degradation. While traditional servo-control systems of wind turbines, such as individual pitch control (IPC) [1], can reduce platform motions and tower loads through multi-objective optimization below the cut-out wind speed (i.e., during operational phases), floating wind turbines encountering extreme events like typhoons will shut down with blades feathered. This necessitates additional control devices (e.g., dampers) to attenuate structural vibrations, especially for highly flexible tower structures.

Initially, Stewart and Lackner [2] recommended installing two linear tuned mass dampers (TMDs) in the fore-aft and lateral directions of the tower. Subsequently, Sun and Jahangi [3] developed a three-dimensional pendulum-type TMD and conducted a comparative analysis of its vibration suppression performance on the towers. Existing studies have rarely discussed the vibration control effectiveness under typhoon events. There is an urgent need to investigate the optimal vibration control for FOWT under offshore extreme events.

Thus, the reliability of the nacelle-installed control device is assessed via parameter optimization under two typhoon scenarios. The remainder of this paper is structured as follows: Section 2 introduces the modeling of the FOWT-TMDI system. Section 3 introduces the extreme wind-wave loads. In Section 4, extreme wind-wave fields of different typhoon events in a specific sea area are simulated, and numerical analyses are conducted to compare the reliability of control performance between the different scenarios. Concluding remarks are presented in Section 5.

2 MODELING OF THE FOWT-TMDI SYSTEM

2.1 Modeling of the FOWT-TMDI

The coordinate system is established based on the schematic diagram of the dynamic model shown in Fig.1. The origin of the inertial coordinate system ($X_1X_2X_3 - G$) is coincident with point G at $t = 0$. The $X_1 - X_2$ plane is defined as the zero potential energy plane for the system's gravitational potential, representing the mean sea level (MSL). In the figure, G_p, G_nc, and G_r denote the centroid positions of the platform, nacelle, and rotor, respectively. The floating platform is assumed to be a rigid body, while the hub and nacelle are also treated as two separate rigid bodies. The floating platform's motion is described using six degrees of freedom in the ($X_1X_2X_3 - G$) coordinate system. Both the tower and blades are modeled as elastic cantilever beams. The tower's degrees of freedom (fore-aft and side-side) are defined in a local coordinate system with its origin at the central point o of the tower base ($oX_1^{'}X_2^{'}X_3^{'}$). Blade degrees of freedom (3 flap-wise displacements and 3 edge-wise displacements) are described using a moving blade coordinate system ($o^{'}x_1^{'}x_2^{'}x_3^{'}$) with its origin at the center of the hub. Additionally, $q_\mathrm{R}(t)$ is defined as the azimuth angle of blade 1 relative to the nacelle's local coordinate system, and Ω represents the actual rotor rotational speed. The TMDI is installed within the nacelle, with a rotary device at its base to allow angle adjustment. It is composed of a parallel spring (stiffness k_d), a mass block (m_d), a damper (damping coefficient c_d), and an inerter (inerter coefficient b_d). Thus, the displacement degree-of-freedom vector of the TMDI mass in the fixed global coordinate system is denoted as

$$\mathbf{r}_\mathrm{D}(t) = \begin{bmatrix} q_\mathrm{su}(t) \\ q_\mathrm{sw}(t) \\ q_\mathrm{he}(t) \end{bmatrix} + \mathbf{T}_\mathrm{P}\left(\begin{bmatrix} u_\mathrm{Tfa}(l_\mathrm{T},t) \\ u_\mathrm{Tss}(l_\mathrm{T},t) \\ l_\mathrm{T}+h_\mathrm{T} \end{bmatrix} + \mathbf{T}_\mathrm{T} \begin{bmatrix} q_\mathrm{d}(t)\cos(\alpha(t)) \\ q_\mathrm{d}(t)\sin(\alpha(t)) \\ 0 \end{bmatrix} \right) \tag{1}$$

where l_T denotes the tower length; α is the angle between the direction of motion of the mass block and the x_1-axis; h_T denotes the height from the MSL to the base of the tower; $q_\mathrm{su}(t)$, $q_\mathrm{sw}(t)$ and $q_\mathrm{he}(t)$

denote surge, sway and heave motions of the platform, respectively. $u_{\mathrm{Tfa}}(l_{\mathrm{T}})$ and $u_{\mathrm{Tss}}(l_{\mathrm{T}})$ denote the deflection of the tower at the position l_{T} along the fore-aft and side-side directions, respectively; $\mathbf{T}_{\mathrm{T}}$ denotes the coordinate transform matrix from the nacelle or hub to the tower coordinate system; $\mathbf{T}_{\mathrm{P}}$ denotes the coordinate transform matrix from the platform to the global coordinate system.

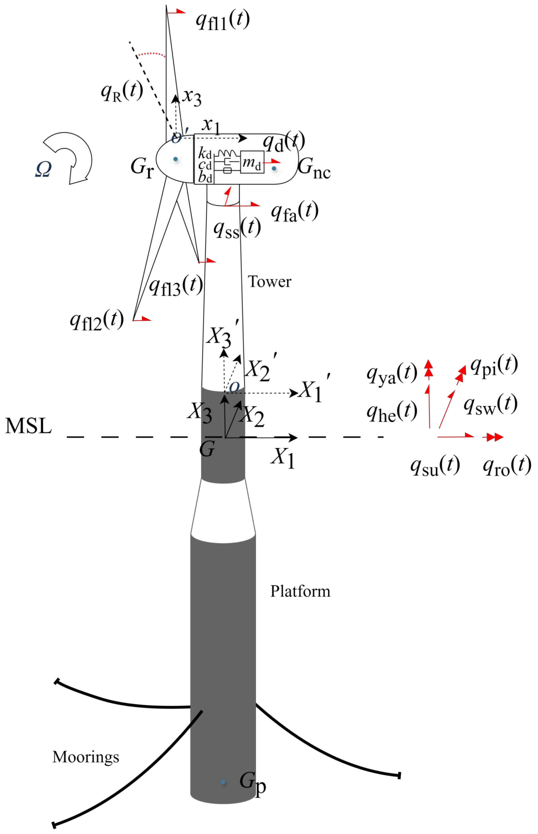

Figure 1: Coordinates and DOFs of the FOWT-TMDI system

The equations of motion of the system are derived using the Euler-Lagrange method as [4]

$$\mathbf{M}(t)\ddot{\mathbf{q}}(t) + \mathbf{C}(t)\dot{\mathbf{q}}(t) + \mathbf{K}(t)\mathbf{q}(t) = \mathbf{f}_{\mathrm{hdys}} + \mathbf{f}_{\mathrm{moor}} + \mathbf{f}_{\mathrm{hydd}} + \mathbf{f}_{\mathrm{aero}} \tag{2}$$

where $\mathbf{M}(t)$, $\mathbf{C}(t)$ and $\mathbf{K}(t)$ represent the mass, damping, and stiffness matrices of the system, respectively; $\mathbf{q}$ denotes a vector of 16 degrees-of-freedoms (DOFs). On the right side, there are vectors of hydrostatic loads $\mathbf{f}_{\mathrm{hdys}}$, mooring loads $\mathbf{f}_{\mathrm{moor}}$, hydrodynamic loads $\mathbf{f}_{\mathrm{hydd}}$, aerodynamic loads $\mathbf{f}_{\mathrm{aero}}$.

2.2 TMDI with active orientation adjustment

This study employs a ball screw mechanism to convert linear motion induced by structural vibrations into high-speed rotational motion of a flywheel, thereby achieving the inertial mass amplification effect [5]. Simultaneously, the high-speed rotational motion generates shear forces in the viscous fluid within the cylinder, producing a damping effect. As shown in Fig.2, the active rotary device enables the entire TMDI to rotate, thereby dissipating vibration energy from the floating tower in multiple directions. This alignment ensures the mass block's motion is coincident with the tower's vibration direction.

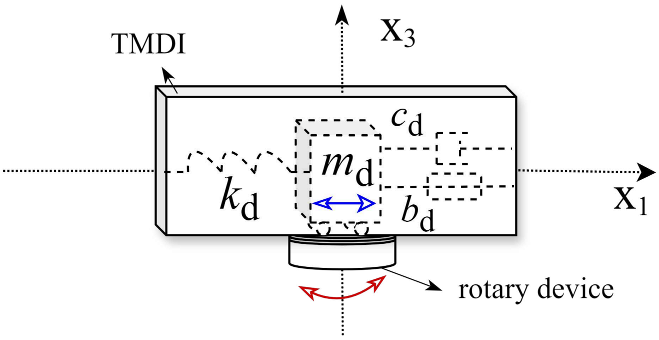

Figure 2: Schematic of the hybrid TMDI

The TMDI can be simplified as a rotatable rectangular mass, whose rotational motion is described by a second-order linear system as follows:

$$J\ddot{\gamma}(t) + B\dot{\gamma}(t) = \tau \tag{3}$$

$$J = \frac{m}{12}\left(a^2 + b^2\right) \tag{4}$$

where $\gamma \in [-90^\circ, 90^\circ]$ is the angle between the long side of the rectangular mass block and the $\mathbf{X}_1$-axis; J is the moment of inertia of the rectangular mass block; B is the damping coefficient of the system; τ is the torque applied to the system; m is the total mass of the TMDI; a is the length of the rectangular block; and b is the width of the rectangular block.

To ensure the TMDI's work angle follows the real-time vibration displacement direction of the tower, a dedicated controller is required. First, the angle information monitored by sensors at the tower top is input into the feedback controller. Meanwhile, the measured working angle of the TMDI is supplemented for feedback processing. Then, the controller sends a saturated output signal to the rotary device to align the mass block's motion direction with the tower's vibration direction. Finally, a closed-loop control system is formed. The corresponding control force required for the output, derived using the backstepping method [6], is given by the following equation:

$$\tau = J\left(\alpha - \gamma\right) + J\ddot{\alpha} + Jk_1\left(\dot{\alpha} - \dot{\gamma}\right) + B\dot{\gamma} + Jk_2\left(\dot{\alpha} + k_1 - \dot{\gamma}\right) \tag{5}$$

where k_1 and k_2 are the controller gains, α is actual angle of the tower top vibration direction.

3 MODELING OF TYPHOON AND WAVE LOADS

The Holland model is employed to model the typhoon wind field in this study, where the radial profile of typhoon wind speed is given by [7]

$$V(r) = \sqrt{\frac{B(\Delta P)}{\rho}\left(\frac{R_{mw}}{r}\right)^B \exp\left[-\left(\frac{R_{mw}}{r}\right)^B\right] + \frac{r^2 f^2}{4}} - \frac{rf}{2} \tag{6}$$

where f is the Coriolis parameter and ρ is air density. ΔP represents the difference between the ambient pressure and the lowest pressure in the typhoon center. r is radial distance from the center of the storm, R_{mw} is the radius of maximum winds, B is the form factor.

The time-varying mean wind generated by a typhoon can be expressed as the vector sum of a gradient wind component related to the typhoon itself and a background wind component induced by the typhoon's overall translation. Over a short period, the typhoon transit relative to the FOWT's position can be approximated as linear motion, and the schematic diagram for calculating the time-varying mean wind speed is shown in Fig.3. It is assumed that the typhoon translation direction aligns with the horizontal-axis, and the coordinate system is fixed at the typhoon's center o. At the initial time $t = 0$, the observation point P (i.e., the FOWT location) has coordinates (d_o, d_e), where d_e is the offset distance from P to the typhoon track, and d_o is the initial horizontal distance from P to the typhoon center. As the typhoon translates, the wind speed at point P changes, and the time-varying mean wind at the reference point on the ground generated by the typhoon is calculated by the following equation:

$$\vec{U}\,(t) = \alpha_r \vec{V}\,(t) + \alpha_t \vec{V_t}\,(t) \tag{7}$$

where α_r is the ground wind reduction factor, and α_t is the reduction factor for the overall moving speed of the typhoon. V_t is the overall moving speed of the typhoon.

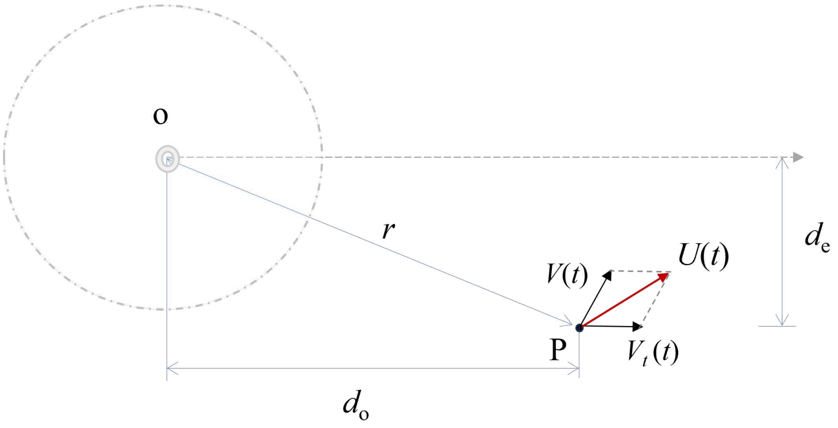

Figure 3: Schematic diagram for the time-mean wind speed

The turbulent wind field is simulated using the IEC-recommended Kaimal spectrum and extreme turbulence model. After reducing the dimensionality of random phase angle variables in the traditional spectral representation method, the fluctuating wind speed at a point in the turbulent wind field can be represented as [8]

$$v_i(t) = \sum_{m=1}^{i}\sum_{k=1}^{N_v} |H_{im}(w_{mk})| \sqrt{\Delta w} \left[R_{mk}\cos(w_{mk}t) - I_{mk}\sin(w_{mk}t)\right], \Delta w = \frac{w_{vu}}{N_v} \tag{8}$$

$$\bar{R}_{mk} = \sqrt{2}\cos(m\Theta_1 + \varphi_c)\sin(k\Theta_2 + \varphi_c) \tag{9}$$

$$\bar{I}_{mk} = \sqrt{2}\sin(m\Theta_1 + \varphi_c)\cos(k\Theta_2 + \varphi_c) \tag{10}$$

where H_{im} denotes a lower triangular matrix, which is derived from a Cholesky decomposition of cross power spectrum matrix, e.g., the one-sided Kaimal spectrum; w_{mk} denotes the double-indexed frequency; w_{vu} denotes the upper of circular frequency of wind spectrum; N_v denotes the number of discrete frequencies of wind spectrum; $\left\{\bar{R}_{mk}, \bar{I}_{mk}\right\}$ represent the set of orthonormal stochastic functions, here, it can be transformed into the orthogonal set of random variables $(\{R_{mk}, I_{mk}\})$ through a deterministic one-to-one mapping; Θ_1 and Θ_2 denote the elemental random variables; φ_c denotes a constant which is typically valued by $\varphi_c = \frac{\pi}{4}$. The total wind speed at the spatial point is obtained by summing the fluctuating wind speed with the aforementioned time-varying mean wind speed. Finally, the wind speed loads on the blades are derived using the actuator line method and blade element momentum (BEM) theory.

Due to the small influence of the spar structure on the flow field, i.e., the ratio of the characteristic length of the floating body structure to the wavelength of the waves being 0.2, the effects of diffraction and radiation can be simplified. The hydrodynamic loads can be calculated by Morisonss formula. To calculate the water particle velocity and acceleration required for Morison's equation, here similarly employs the dimensionality-reduced spectral representation method based on the JONSWAP spectrum to express the water particle velocity and acceleration at the point $(X_1, X_2 = 0, X_3 \leq 0)$ in the global coordinate system as [9]

$$v_{wh}(X_1, X_3, t) = \frac{w_s \cosh[k_s(X_3 + h_\mathrm{D})]}{\sinh(k_s h_\mathrm{D})} \eta(X_1, t) \tag{11}$$

$$a_{wh}(X_1, X_3, t) = \frac{{w_s}^2 \cosh[k_s(X_3 + h_\mathrm{D})]}{\sinh(k_s h_\mathrm{D})} \dot{\eta}(X_1, t) \tag{12}$$

$$\bar{X}_s = \cos(s\Theta_3) + \sin(s\Theta_3) \tag{13}$$

$$\bar{Y}_s = \cos(s\Theta_4) + \sin(s\Theta_4) \tag{14}$$

$$\eta(X_1 = 0, t) = \sum_{s=1}^{N_\eta} \sqrt{2S_\mathrm{JON}(w_s)\Delta w}\, [\cos(w_s t)X_s + \sin(w_s t)Y_s] \tag{15}$$

where w_s is the wave frequency; k_s is the wave number; h_D is the water depth; s is the sth frequency component; η represents the irregular wave surface elevation given by linear wave theory; S_JON is the two-sided wave spectrum. $\{X_s, Y_s\}$ represent the sets of orthonormal stochastic functions, the elementary random variables (Θ_3 and Θ_4) are mutually independent and both submit to uniform distribution in the range $[0, 2\pi]$.

4 NUMERICAL EXAMPLES

This section optimizes the control device parameters for different scenarios, evaluates the FOWT-hybrid-TMDI system's vibration control performance during two typhoon events, and compares their reliability under varying typhoon impacts.

4.1 Simulation of the two typhoon events

Two typical super typhoon events are selected from the CMA Tropical Cyclone Best Track Dataset, with their tracks shown in Fig.4. Super Typhoon Chan-hom (1509) originated east of the Philippines in the northwestern Pacific on 30 June 2015, intensified into a super typhoon by 8 July, and reached a maximum sustained wind speed of 55 m/s. It traversed the East China Sea before making landfall in Zhejiang Province. Severe Typhoon Muifa (2212) formed in the same region on 6 September 2022, peaking with winds of 52 m/s near its center.

Two extreme scenarios were selected based on the closest approach of each typhoon eye to the FOWT (point P, 29.8°N and 123.1°E), with the total transit time (duration within the typhoon's influence area) simulated for 15 minutes. Accordingly, specific positions are set as shown in Fig.5. For Chan-hom, the closest approach occurred around 00:00 on July 11, at coordinates 28.6°N and 122.8°E. For Muifa, the closest approach occurred around 06:00 on September 14, at coordinates 28.8°N and 122.7°E. Additionally, to obtain the corresponding sea state parameters for wave loads simulation, these two moments' sea state parameters (significant wave height H_s, wave peak period T_p and wind-wave angle ϕ) were obtained from the ERA5 database. Detailed information is presented in Table 1. Typical wind speed time histories at the hub and wave surface elevation, generated considering random variables (Θ_1, Θ_2, Θ_3 and Θ_4) from different random seeds, are shown in Fig.6 and Fig.7.

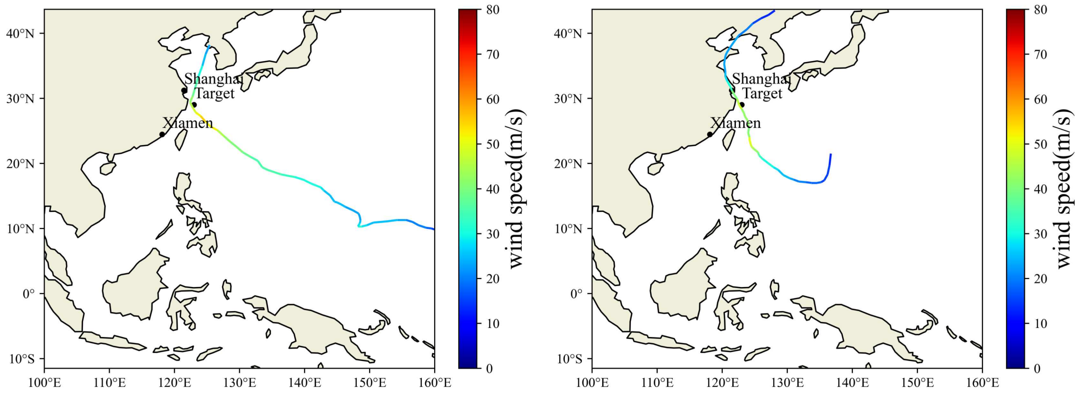

(a) Track map of Typhoon Chan-hom (b) Track map of Typhoon Muifa

Figure 4: Wind speed at different locations and at different times

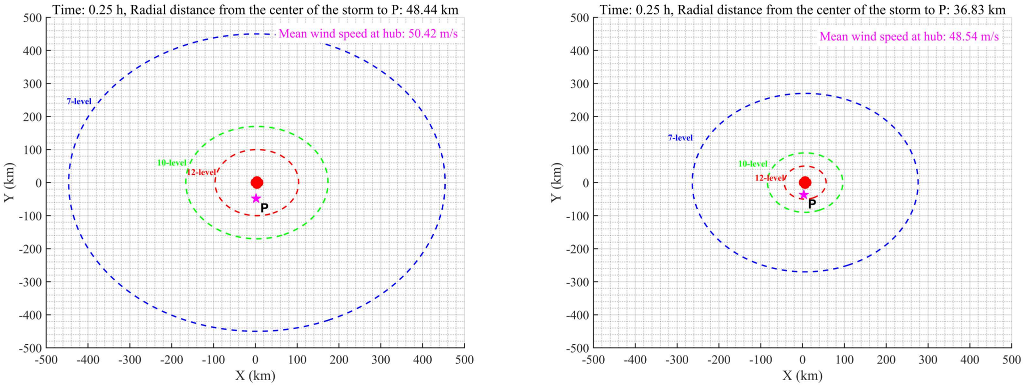

(a) Typhoon Chan-hom is passing through (b) Typhoon Muifa is passing through

Figure 5: Extreme conditions in transit of the two typhoons

Table 1: Table of parameters related to the two extreme cases

Events	R_{mw} (km)	V_t (km/h)	ΔP (hPa)	d_e (km)	d_o (km)	H_s (m)	T_p (s)	ϕ (rad)
Chan-hom	58.3	15	75	48.4	1.875	9.5	11.03	0.58
Muifa	64	25	65	36.7	3.125	8.4	7.8	0.07

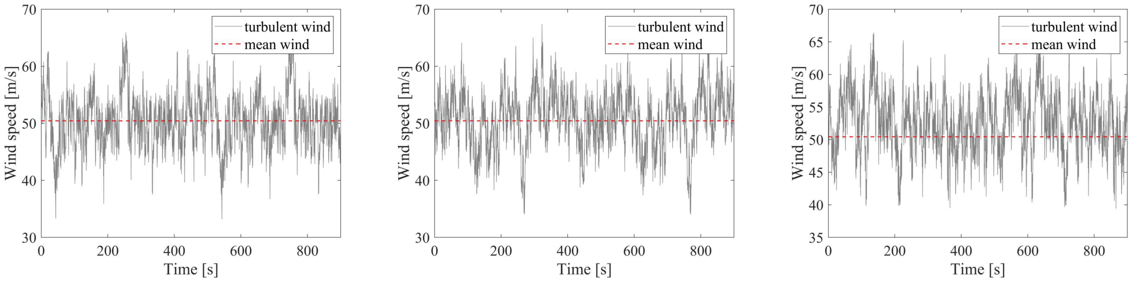

(a) Chan-hom 1 (b) Chan-hom 2 (c) Chan-hom 3

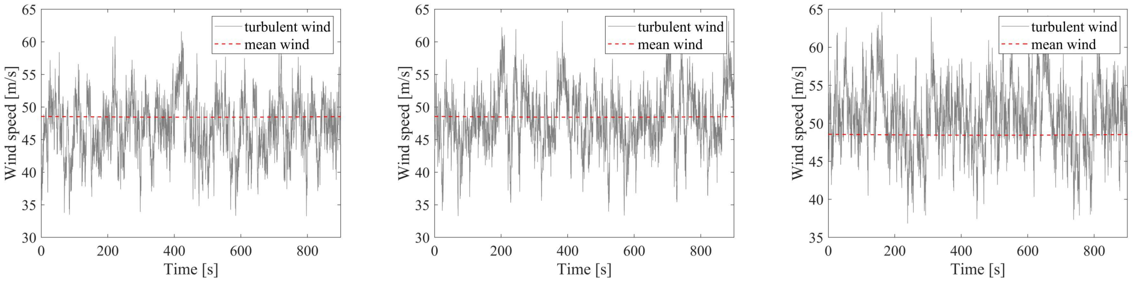

(d) Muifa 1 (e) Muifa 2 (f) Muifa 3

Figure 6: Wind speed time history generated by different random seeds

4.2 Parameters optimization

To fully account for the randomness of generated samples (i.e., different random seeds), the surrogate model combined with a genetic algorithm is used here to optimize the TMDI-related parameters for robustness. The optimization problem is formulated as follows:

$$\beta_{\mathrm{d}} = \frac{b_{\mathrm{a}}}{m_0}, \quad \alpha_{\mathrm{d}} = \frac{w_{\mathrm{d}}}{w_{\mathrm{t}}}, \quad \zeta_{\mathrm{d}} = \frac{c_{\mathrm{d}}}{2m_{\mathrm{d}}w_{\mathrm{d}}} \tag{16}$$

$$\text{find} \quad d = \{\beta_{\mathrm{d}}, \alpha_{\mathrm{d}}, \zeta_{\mathrm{d}}, k_1, k_2\} \tag{17}$$

$$\text{minimize} \quad f = \frac{E(D_{\text{tower}})}{a} + \frac{E(A_{\text{platform}})}{b} \tag{18}$$

$$\text{s.t.} \quad d_{\min} \le d \le d_{\max} \tag{19}$$

where D_{tower} denotes the total displacement at the tower top (the resultant of different directional displacements) under environmental variables; A_{platform} denotes the total angle of the platform under environmental variables. Values of a and b are empirically set to be close to the maximum values of D_{tower} and A_{platform}, respectively. β_{d}, α_{d}, and ζ_{d} are the inertance-to-mass ratio, frequency ratio, and damping ratio of the TMDI, respectively. w_{d} is the natural frequency of the damper, w_{t} is the natural frequency of the tower; c_{d} is the damping coefficient of the damper, b_{a} is the inerter coefficient, and m_{d} represents the mass block mass (it is 1000 kg here). $E(\cdot)$ represents the arithmetic mean over 10,000 random seeds (computed using a neural network surrogate model during the optimization process). Optimal parameters under different typhoon events are shown in Table 2.

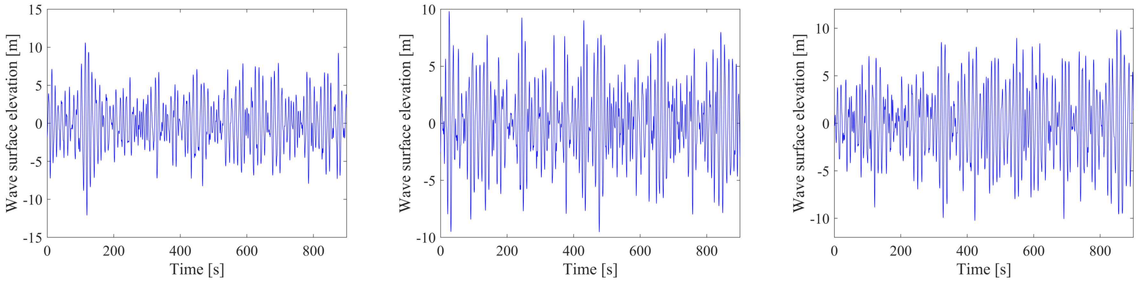

(a) Chan-hom 1 (b) Chan-hom 2 (c) Chan-hom 3

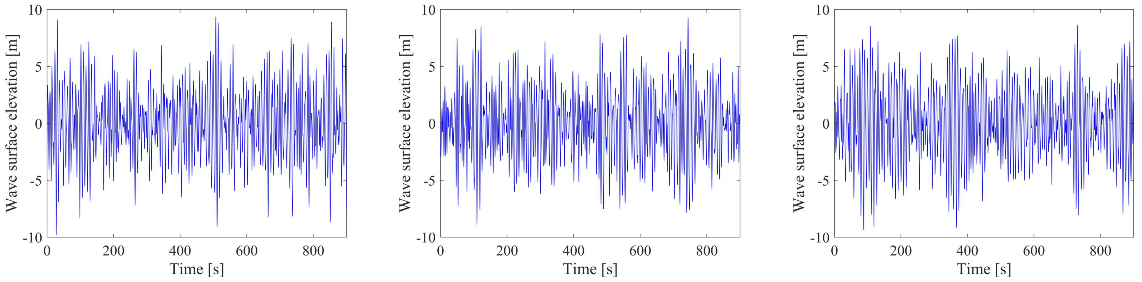

(d) Muifa 1 (e) Muifa 2 (f) Muifa 3

Figure 7: Wave surface elevation generated by different random seeds

Table 2: Table of parameters related to the two extreme cases

Events	β_{d}	α_{d}	ζ_{d}	k_1	k_2
Chan-hom	0.987	3.071	14.012	6.089	5.779
Muifa	0.880	5.954	7.539	2.149	4.536

4.3 Results and discussions

The cumulative distribution functions (CDFs) and probability density functions (PDFs) of the tower total displacement and platform tilt angle, computed using the Probability Density Evolution Method (PDEM) [10], are presented in Fig.8 and Fig.9.

From the displacement results, the curves representing the PDF and CDF shift significantly to the left after deploying the TMDI, indicating a notable reduction in the mean value of extreme tower top displacements when the control device is activated. For the floating platform, the TMDI also mitigates the platform's inclination angle to a certain extent. More importantly, the optimal TMDI parameters optimized under the typhoon Chan-hom scenario are not suitable for the typhoon Muifa environment. The comparison reveals a significant difference in tower top displacements, while the difference in the floating platform's tilt angle is less pronounced.

To some extent, hybrid TMDI optimized for worst-case scenarios cannot guarantee optimal control performance. For example, Typhoon Chan-hom, as mentioned in this study, induces higher wind speed and wave height for the FOWT at the target site compared to Typhoon Muifa. This can lead to diminished performance of the control device where efforts yield less effective results, or even cause adverse effects such as amplified vibrations under some extreme events.

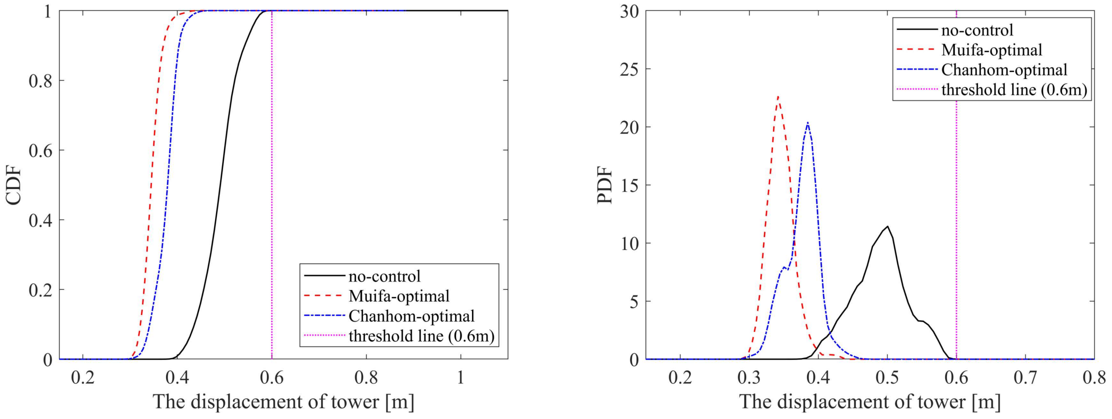

(a) CDF (b) PDF

Figure 8: The tower diplacement under Muifa

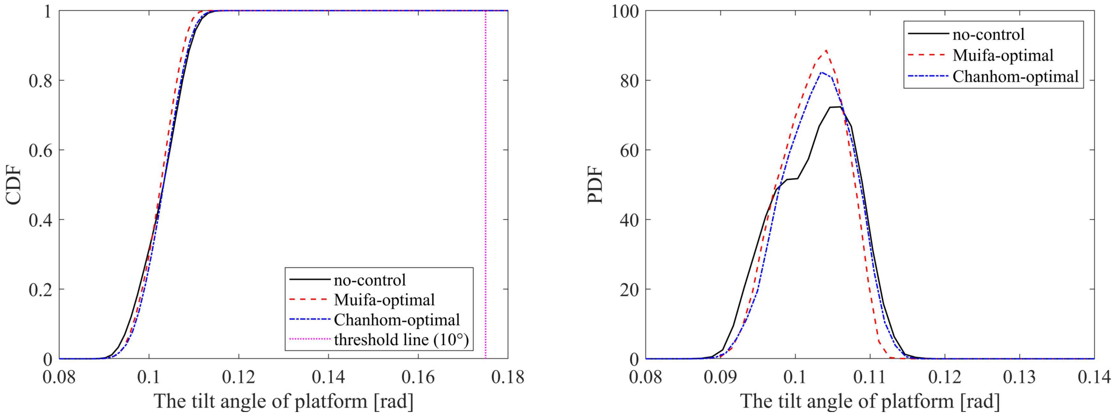

(a) CDF (b) PDF

Figure 9: The tilt angle under Muifa

5 CONCLUSIONS

- Under typhoon events, the optimized TMDI hybrid control effectively mitigates adverse vibrations in the floating wind turbine structure in terms of reliability. The suppression of tower top displacement is most pronounced, while it also exhibits effectiveness in reducing the floating platform's tilt angle.
- The design and control effectiveness of the hybrid TMDI exhibit variability due to typhoon event differences. Future research should therefore focus on the cumulative impact of typhoons across the entire sea area affecting the specific site. For example, conducting reliability-based optimization design after establishing integrated typhoon-wave fields.

REFERENCES

[1] H. Namik, K. Stol, Performance analysis of individual blade pitch control of offshore wind turbines on two floating platforms, Mechatronics 21 (4) (2011) 691–703.

[2] M. A. Lackner, M. A. Rotea, Passive structural control of offshore wind turbines, Wind Energy 14 (3) (2011) 373–388.

[3] C. Sun, V. Jahangiri, Bi-directional vibration control of offshore wind turbines using a 3d pendulum tuned mass damper, Mechanical Systems and Signal Processing 105 (2018) 338–360.

[4] Y. Peng, T. Chang, Reliability-based design optimization of tuned mass-damper-inerter for vibration mitigation of spar-type floating offshore wind turbines, Ocean Engineering 310 (2024) 118630.

[5] K. Ikago, K. Saito, N. Inoue, Seismic control of single-degree-of-freedom structure using tuned viscous mass damper, Earthquake Engineering and Structural Dynamics 41 (3) (2012) 453–474.

[6] X. Shao, J. Liu, H. Wang, Robust back-stepping output feedback trajectory tracking for quadrotors via extended state observer and sigmoid tracking differentiator, Mechanical Systems and Signal Processing 104 (2018) 631–647.

[7] A. C. Phadke, C. D. Martino, K. F. Cheung, S. H. Houston, Modeling of tropical cyclone winds and waves for emergency management, Ocean Engineering 30 (4) (2003) 553–578.

[8] Z. Liu, Z. Liu, Y. Peng, Simulation of multivariate stationary stochastic processes using dimension-reduction representation methods, Journal of Sound and Vibration 418 (2018) 144–162.

[9] Z. Liu, W. Liu, Y. Peng, Random function based spectral representation of stationary and non-stationary stochastic processes, Probabilistic Engineering Mechanics 45 (2016) 115–126.

[10] J. Li, J. Chen, Stochastic Dynamics of Structures, John Wiley and Sons, 2009.